Chemical Engineering Journal 429 (2022) 132396

Contents lists available at ScienceDirect

Chemical Engineering Journal

journal homepage: www.elsevier.com/locate/cej

Multidimensional synergistic architecture of Ti_3C_2 MXene/CoS_2@N-doped carbon for sodium-ion batteries with ultralong cycle lifespan

Pengfei Huang, Hangjun Ying, Shunlong Zhang, Zhao Zhang, Wei-Qiang Han *

School of Materials Science and Engineering, Zhejiang University, Hangzhou 310027, China

ARTICLE INFO

Keywords:
Ti_3C_2 MXene
CoS_2
Multidimensional synergistic architecture
Sodium-ion batteries
Superior cycle lifespan

ABSTRACT

Sodium-ion batteries (SIBs) based on conversion-type anode materials exhibit great prospect in the field of large-scale energy storage because of their superior sodiation capacities and low costs. However, poor charge transfer kinetics and short cycle life induced by huge volume change remain two great challenges. Herein, a multidimensional synergistic structure of few-layered Ti_3C_2 MXene/CoS_2@N-doped porous carbon (f-Ti_3C_2/CoS_2@NPC) is rationally designed as SIBs anodes, where N-doped porous carbon matrix-encapsulated ultrafine CoS_2 nanoparticles are anchored on few-layered Ti_3C_2 MXene via Ti—O—C bonds. The synergistic effects among each component greatly inhibit the aggregation of CoS_2 nanoparticles (CoS_2 NPs), readily build a long-range electron/Na^+ conductive network and effectively provide a dual protection effect on CoS_2 NPs during sodiation/desodiation process. Consequently, the f-Ti_3C_2/CoS_2@NPC anode delivers a high-rate performance (282.6 mAh g^{-1} at 10 A g^{-1}) and superior cyclability (200.6 mAh g^{-1} at 2 A g^{-1} after 1500 cycles). Furthermore, $Na_3V_2(PO_4)_3$//f-Ti_3C_2/CoS_2@NPC full cells can release a high reversible capacity and good cyclability (325.8 mAh g^{-1} at 200 mA g^{-1} after 50 cycles), demonstrating great potential in practical application. This work further broadens the scope of multidimensional synergistic architectures and may inspires more research on MXene-based multidimensional structure for high-performance SIBs.

1. Introduction

Large-scale energy storage systems (ESSs) are becoming increasingly significant to smoothly integrate the renewable energy sources, which is expected to be the most promising alternatives to fossil fuels [1–2]. Among different energy storage devices, secondary batteries have triggered considerable interests owing to their high conversion efficiency, simple maintenance and long cycle life [3–5]. However, the large-scale application of state-of-the-art rechargeable batteries (*i.e.*, lithium-ion batteries) in ESSs fields is greatly restricted by the limited lithium abundance and uneven distribution [6]. Recently, sodium-ion batteries (SIBs) have been massively investigated owing to its low cost and rich sodium resource [7–11]. Unfortunately, large ionic radius of Na^+ (1.02 Å) induces large volume strain during Na^+ insertion/extraction process, resulting in a low sodiation capacity and inferior cyclic performance [12–13], which makes it difficult to design high performance SIBs anodes with durable cyclic performance.

As a new rising star of two-dimensional materials (2D materials), MXenes, generally prepared by HF, LiF + HCl or Lewis-acidic-melt etching, were first discovered in 2011 by the group of Gogotsi and Barsoum [14–16], which have been widely exploited in various fields including catalysis, electromagnetic interference shielding and energy storage [9,17–22]. Particularly, Ti_3C_2 MXene is regarded as an appealing SIBs anode material on account of its large interlayer spacing, high electronic conductivity and low Na^+ diffusion barrier [23–26]. However, its sodium storage performance is considerably plagued by detrimental effect of surface functional groups (–F and –OH) and self-restacking issue of Ti_3C_2 MXene owing to the van der Waals interactions and hydrogen bonds between contiguous nanoflakes [27–29]. Fortunately, few-layered Ti_3C_2 MXene (denoted as f-Ti_3C_2 MXene) fabricated by solution-phase flocculation (SPF) method with 3D porous architecture outperform multi-layered Ti_3C_2 MXene (m-Ti_3C_2 MXene) and restacked Ti_3C_2 MXene [30–31], which is mainly due to the larger specific surface area, rapid Na^+ migration in 3D conductive networks and unique chemisorptive ability [32]. Nevertheless, its further application as SIBs anodes is still hindered by inherently low theoretical capacity (351.8 mAh g^{-1}) [33]. To our relief, negative-charged, hydrophilic surface and large surface area endow f-Ti_3C_2 MXene with

* Corresponding author.
E-mail address: hanwq@zju.edu.cn (W.-Q. Han).

https://doi.org/10.1016/j.cej.2021.132396
Received 9 June 2021; Received in revised form 27 August 2021; Accepted 7 September 2021
Available online 15 September 2021

an immense potential to combine with other high-capacity SIBs anodes [17,24,34], which can remarkably increase specific capacity and improve the cycle stability of the composites.

Owing to low cost, superior theoretical capacity and easily broken metal-sulfur bonds, metal sulfides have been widely regarded as underlying anode materials for SIBs [12,35]. In particular, cobalt disulfide (CoS_2) possesses high safety and sodiation capacity based on four-electron reaction mechanism [36], exhibiting a great application prospect. Nevertheless, poor cyclic stability still remains a formidable hindrance caused by drastic volumetric expansion/shrinkage of CoS_2 nanoparticles (CoS_2 NPs) during Na^+ insertion/extraction process [37]. Embedding CoS_2 NPs in a conductive carbon network is an effective approach to address above issue [38–40]. Currently, zeolitic imidazolate framework-67 (ZIF-67) are used to prepare porous carbon-encapsulated CoS_2 NPs (denoted as CoS_2@porous carbon) and the introduction of carbon species can largely enhance the electronic conductivity and reduce the interfacial resistance of hybrids [36], which is beneficial for accomplishing outstanding rate capability. However, CoS_2@porous carbon composites are still unable to achieve ultralong cyclability due to the breakage of protective porous carbon layer (with low elastic modulus) resulted from large volume expansion of CoS_2 NPs during cyclic process [41–45], which cannot meet the demand of prolonged cycle life of ESSs. Undoubtedly, structural design on CoS_2-based anode materials is still needed to be further enhanced. Based on remarkable electrochemical performance of MXene/conversion-type hybrid anode materials owing to favorable stress release ability of MXene [8–9,46], it is anticipated that loading CoS_2@porous carbon composites on f-Ti_3C_2 MXene can exceedingly relieve large volume change of CoS_2 NPs and fully combine their respective advantages, thus contributing to high structural stability and ultralong cycle lifespan [4,27,47–48]. However, to the best of our knowledge, rational design of such a multidimensional synergistic structure as SIBs anodes has not been reported yet.

Herein, we first prepare f-Ti_3C_2 MXene without restacking phenomenon via NH_4^+-assisted SPF method and then delicately construct f-Ti_3C_2/CoS_2@N-doped porous carbon (denoted as f-Ti_3C_2/CoS_2@NPC) composites for sodium storage via *in situ* carbonization and sulfurization treatment of f-Ti_3C_2/ZIF-67 hybrids, where N-doped porous carbon-encapsulated CoS_2 NPs (denoted as CoS_2@NPC) are supported by f-Ti_3C_2 MXene. The elaborately designed hierarchical architecture affords multiple merits: i) Ultrafine CoS_2 NPs can extremely shorten Na^+ diffusion length and utilize more electrochemical active sites to obtain a higher capacity; ii) N-doped porous carbon (NPC) as an initial buffer matrix can greatly improve the electronic conductivity of the hybrids, inhibit the self-aggregation and partly reconcile significant volume change of CoS_2 NPs; and iii) f-Ti_3C_2 MXene as a principal protection framework can not only prevent NPC layer from cracking, forming a dual release path for the inevitable stress of CoS_2 NPs during repeated Na^+ insertion/extraction process, but also possess enough contact between electrode and electrolyte and speed up Na^+/electron transport to readily build a long-range conductive network. As a result, f-Ti_3C_2/CoS_2@NPC composites exhibit extraordinary rate performance and superior cyclability (200.6 mAh g^{-1} at 2 A g^{-1} after 1500 cycles and 104.1 mAh g^{-1} after 8000 cycles at 10 A g^{-1}) as SIBs anodes. More importantly, a full cell system assembled by $Na_3V_2(PO_4)_3$ cathode and f-Ti_3C_2/CoS_2@NPC anode achieves a capacity of 325.8 mAh g^{-1} after 50 cycles at 200 mA g^{-1} with an output voltage of 2.1 V.

2. Experimental

2.1. Synthesis of m-Ti_3C_2 MXene and f-Ti_3C_2 MXene

The m-Ti_3C_2 MXene powders were obtained by etching Al layers from Ti_3AlC_2 MAX (>98% purity, Forsman Co., Ltd). After the etching, centrifugation and washing process, the m-Ti_3C_2 MXene can be readily prepared. The f-Ti_3C_2 MXene powders were prepared by NH_4^+-assisted SPF strategy, including tetramethylammonium hydroxide (TMAOH, 25%) intercalation, ultrasonication and centrifugation (3500 rpm, 10 min) as well as the addition of NH_4^+ to the collected supernatant. The detailed procedure can refer to our previously reported works [49].

2.2. Synthesis of f-Ti_3C_2/ZIF-67

Typically, 80 mg of f-Ti_3C_2 MXene powders were dispersed in 30 mL of methanol by ultrasonication for 30 min. 2 mmol of $Co(NO_3)_2{\cdot}6H_2O$ was added to 20 mL of methanol to form solution by magnetic stirring for 1 h. 16 mmol of 2-methylimidazole was dissolved in 40 mL of methanol by stirring for 1 h. As followed, the $Co(NO_3)_2{\cdot}6H_2O$ solution was slowly added to the f-Ti_3C_2 MXene dispersion by stirring for 1 h and the Co^{2+} ions can be absorbed by the negative group (−F, −O and −OH) of f-Ti_3C_2 MXene [14,24]. The 2-methylimidazole solution which can coordinate with Co^{2+} ions to form ZIF-67 was quickly poured into the above f-Ti_3C_2/$Co(NO_3)_2{\cdot}6H_2O$ dispersion with vigorous stirring for 8 h. Finally, f-Ti_3C_2/ZIF-67 powders were harvested by centrifugation (8000 rpm, 10 min), washing with methanol for three times and vacuum-drying at 80 ℃ for 24 h. The pure ZIF-67 powders were prepared by the same method just without the introduction of f-Ti_3C_2 MXene.

2.3. Synthesis of f-Ti_3C_2/CoS_2@NPC hybrids

The f-Ti_3C_2/CoS_2@NPC hybrids were prepared by carbonization and sulfurization process. First, the f-Ti_3C_2/ZIF-67 composites were carbonized at 550 ℃ for 100 min (heating rate: 1 ℃/min) in a tube furnace under Ar atmosphere to prepare f-Ti_3C_2/Co@NPC hybrids. Then, f-Ti_3C_2/Co@NPC powders and thiourea were put at two separated porcelain boats and the boat for thiourea was placed at the upstream side of the tube furnace. Finally, they were heated at 300 ℃ for 2 h (heating rate: 1 ℃/min) in flowing Ar. The f-Ti_3C_2/CoS_2@NPC powders were harvested after cooling down to ambient temperature under Ar. The N-doped porous carbon coated Co metal nanoparticles (denoted as Co@NPC) and CoS_2@NPC were synthesized through the same strategy. Additionally, pure CoS_2 was purchased from Sinopharm reagent Co., Ltd. and pure f-Ti_3C_2 MXene annealed at 550 ℃ for 100 min under flowing Ar with a heating rate of 1 ℃/min was denoted as f-Ti_3C_2-550.

2.4. Characterization

The crystal structures and compositions of as-prepared samples were tested by a Rigaku MiniFlex 600 X-ray diffractometer (Cu Kα radiation, $2\theta = 2°–70°/80°$) and Raman spectrometer (LabRAM HR Evolution, 532 nm laser). The morphology and microstructure of as-prepared materials were characterized by field-emission scanning electron microscopy (FESEM, SU8010), transmission electron microscopy (TEM, JEM-2100) and high-resolution transmission electron microscopy (HRTEM). The specific surface area and size distribution of those materials were carried out by Micromeritics ASAP 2020 Plus HD88. The surface chemical bonds of the samples were tested by X-ray photoelectron spectrometer (Thermo ESCALAB 250Xi).

2.5. Electrochemical measurements

In order to measure the electrochemical performance, CR2032-type coin cells were assembled in a glovebox. A sodium disc was used as negative electrode and the electrolyte was 1 M $NaClO_4$ in EC: PC (1:1 vol %) with 5 % FEC. The working electrode was composed of 80 wt% active material, 10 wt% Super P and 10 wt% sodium carboxymethylcellulose. The mass loading of active material in the working electrode was about 0.8–1.0 mg cm^{-2}. Galvanostatic charge-discharge (GCD) test and Galvanostatic intermittent titration technique (GITT) test were performed on a Land testing system in the potential range of 0.01–3 V at ambient temperature. Before the GITT test, the coin cells were cycled for one cycle at 50 mA g^{-1}. The specific capacity was calculated based on the total weight of f-Ti_3C_2/CoS_2@NPC hybrids. Cyclic voltammogram (CV)

in a voltage range of 0.01–3 V and electrochemical impedance spectroscopy (EIS) at an open-circuit potential were measured by an electrochemical workstation (Solartron 1470E). For $Na_3V_2(PO_4)_3$ (NVP)//f-Ti_3C_2/CoS_2@NPC full cell, NVP powders were purchased from Shenzhen Kejing Star Technology Co., Ltd. The NVP electrode consisted of 80 wt% NVP, 10 wt% Super P and 10 wt% polyvinylidene fluoride. Before assembling the full cells, f-Ti_3C_2/CoS_2@NPC anodes were activated at 50 mA g^{-1} for 3 cycles in half cells to generate solid electrolyte interface (SEI) layer. The mass ratio of NVP cathode to f-Ti_3C_2/CoS_2@NPC anode was about 5:1 and the potential range was carried out between 0.4 and 3.4 V. The electrolyte was the same as that in half cells. The specific capacities of full cells were calculated by the mass of f-Ti_3C_2/CoS_2@NPC hybrids.

3. Results and discussion

The synthesis process and reaction mechanism of the f-Ti_3C_2/CoS_2@NPC hybrids is illustrated in Fig. 1. Typically, Ti_3AlC_2 powders are etched into accordion-like m-Ti_3C_2 MXene by exposing to aqueous solution of HF for 4 d. Then, f-Ti_3C_2 MXene with 3D porous structure can be obtained by SPF method [49–50], specifically including the process of increasing the interlayer spacing, ultrasonication, centrifugation and the final introduction of NH_4^+ to the collected supernatant. As followed, f-Ti_3C_2/ZIF-67 hybrids are prepared by successively adding the methanol solution of $Co(NO_3)_2{\cdot}6H_2O$ and 2-methylimidazole to f-Ti_3C_2 suspension. After carbonization process under flowing Ar atmosphere, polyhedral ZIF-67 particles are transformed into Co@NPC composites [51]. Subsequently, f-Ti_3C_2/Co@NPC hybrids are sulfurized by

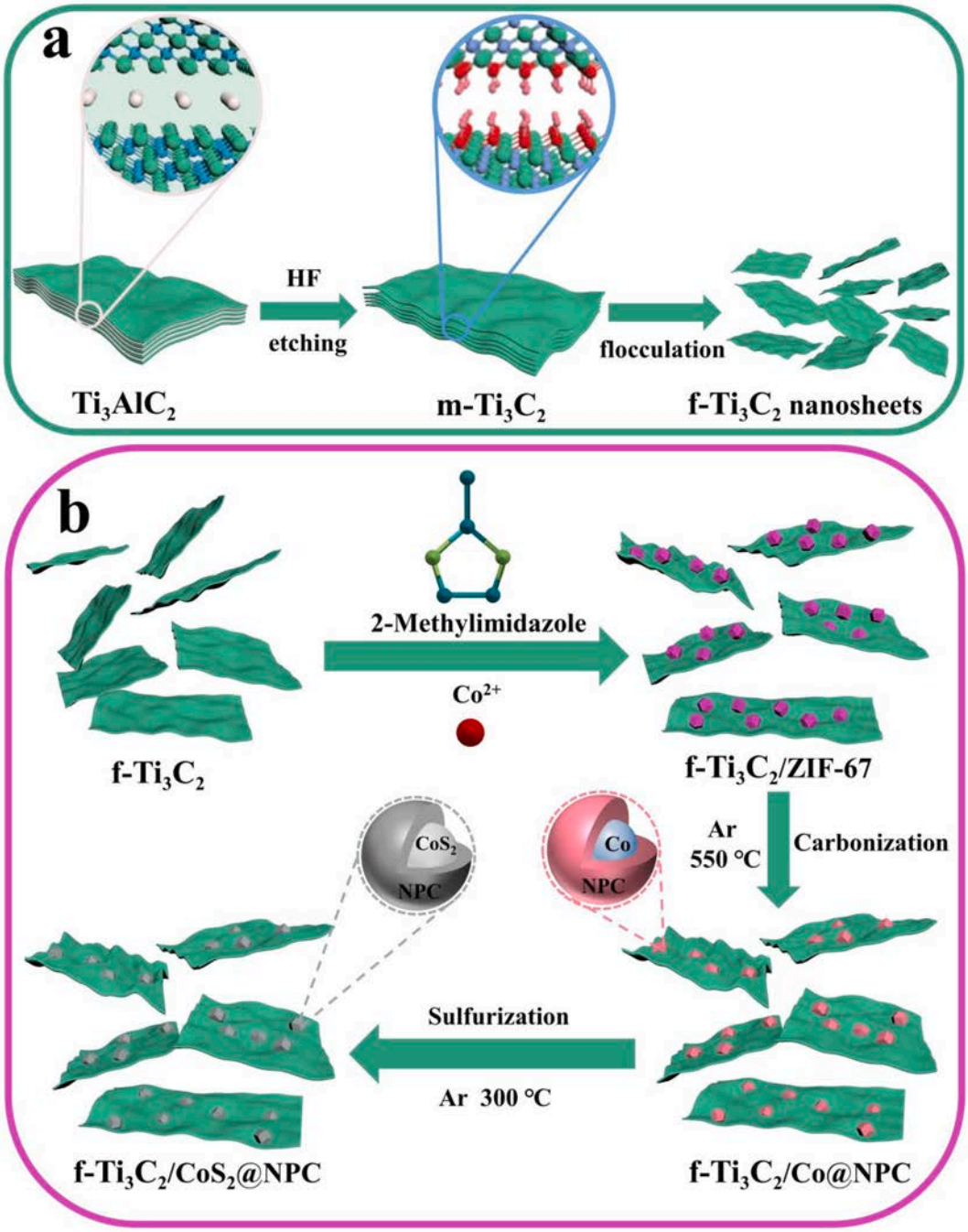

Fig. 1. Schematic illustration of the synthetic process of (a) f-Ti_3C_2 MXene and (b) f-Ti_3C_2/CoS_2@NPC hybrids.

thiourea, which can generate H_2S gas and react with Co particles during the heating process [52]. Finally, multidimensional synergistic nano-architecture of NPC-encapsulated CoS_2 NPs anchored on f-Ti_3C_2 MXene nanosheets is successfully prepared.

Fig. 2a, b and Fig. S1 show the X-ray diffraction (XRD) patterns of obtained materials. As depicted in Fig. 2a, the (104) peak of Ti_3AlC_2 completely vanishes and the strongest (002) peak broadens after HF etching process [53]. The (002) peak left moves to 6.34° for f-Ti_3C_2 MXene, demonstrating an increase of interlayer spacing when compared with that of Ti_3AlC_2 and m-Ti_3C_2 MXene, which can be attributed to the existence of water molecules between layers [54–55]. Pure ZIF-67 possesses sharp and strong diffraction peaks (Fig. S1a), manifesting the highly crystalline structure [56]. For Co@NPC and CoS_2@NPC hybrids, the weak peak located at 25.7° is assigned to (002) plane of carbon (Fig. S1b, c) [57]. Additionally, the existence of carbon in the Co@NPC hybrids can be verified by Raman spectra (Fig. S1d). Two obvious peaks at 1333 and 1588 cm^{-1} are associated with D-band and G-band [3], respectively, and a high I_D/I_G ratio of 0.94 suggest a low graphitization degree for Co@NPC composites. As for f-Ti_3C_2/ZIF-67 hybrids, the XRD pattern comprises pure f-Ti_3C_2 and ZIF-67 and no other peaks belong to new phase (Fig. 2b). After carbonization process at 550 ℃ under Ar atmosphere, the peaks of ZIF-67 disappear and the new peaks at 44.2° and 51.5° corresponding to metal cobalt (JCPDS No. 15-0806) emerge (Fig. 2b and Fig. S1b) [41]. For f-Ti_3C_2/Co@NPC hybrids, the (002) peak of f-Ti_3C_2 MXene right shifts to 6.92° representing the shrinkage of interlayer spacing after carbonization process (Fig. 2b), which is mainly ascribed to the removal of interlayer water [7,58–59]. Additionally, the peak of f-Ti_3C_2/Co@NPC composites situated at 25.6° simultaneously belongs to carbon and TiO_2 (Fig. 2b). The occurrence of TiO_2 indicates that f-Ti_3C_2 MXene has been slightly oxidized. which corresponds to XRD pattern of f-Ti_3C_2 annealed at 550 ℃ (denoted as f-Ti_3C_2-550) (Fig. S1e) [50,60]. Finally, some new peaks located at 27.8°, 32.3°, 36.2°, 39.8°, 46.3°, 54.9° and 62.7° emerge for f-Ti_3C_2/CoS_2@NPC hybrids, corresponding to the (111), (200), (210), (211), (220), (311) and (321) planes of CoS_2 (JCPDS No. 41-1471), respectively [38], indicating the successful formation of CoS_2 after sulfurization process. (Fig. 2b and Fig. S1c).

The N_2 adsorption-desorption isotherm of Co@NPC hybrids illustrated in Fig. S2a indicates a specific surface area of 265.9 $m^2\ g^{-1}$ and pore volume of 0.23 $cm^3\ g^{-1}$, and the pore size distribution is mainly concentrated at 3.61 nm (Fig. S2b), which confirms the formation of porous carbon during carbonization process of ZIF-67. As shown in Fig. S2c-e and Fig. 2c, f-Ti_3C_2 MXene, CoS_2, CoS_2@NPC composites and f-Ti_3C_2/CoS_2@NPC hybrids all exhibit mesoporous structure. More importantly, compared with another three samples, f-Ti_3C_2/CoS_2@NPC hybrids possess adsorption-desorption curve with obvious hysteresis loops and show the largest specific surface area (38.4 $m^2\ g^{-1}$), which can be attributed to the successful preparation of 3D porous multidimensional hierarchical structure. The largest surface area and mesoporous structure of f-Ti_3C_2/CoS_2@NPC hybrids can provide a large electrode/electrolyte interface as well as promote Na^+ transport in electrolyte [61–64], contributing to enhanced electrochemical performance. Fig. 2d exhibits Raman spectra of f-Ti_3C_2 MXene and f-Ti_3C_2/CoS_2@NPC hybrids. The I_D/I_G ratio of f-Ti_3C_2 MXene is 0.84, indicating a relatively

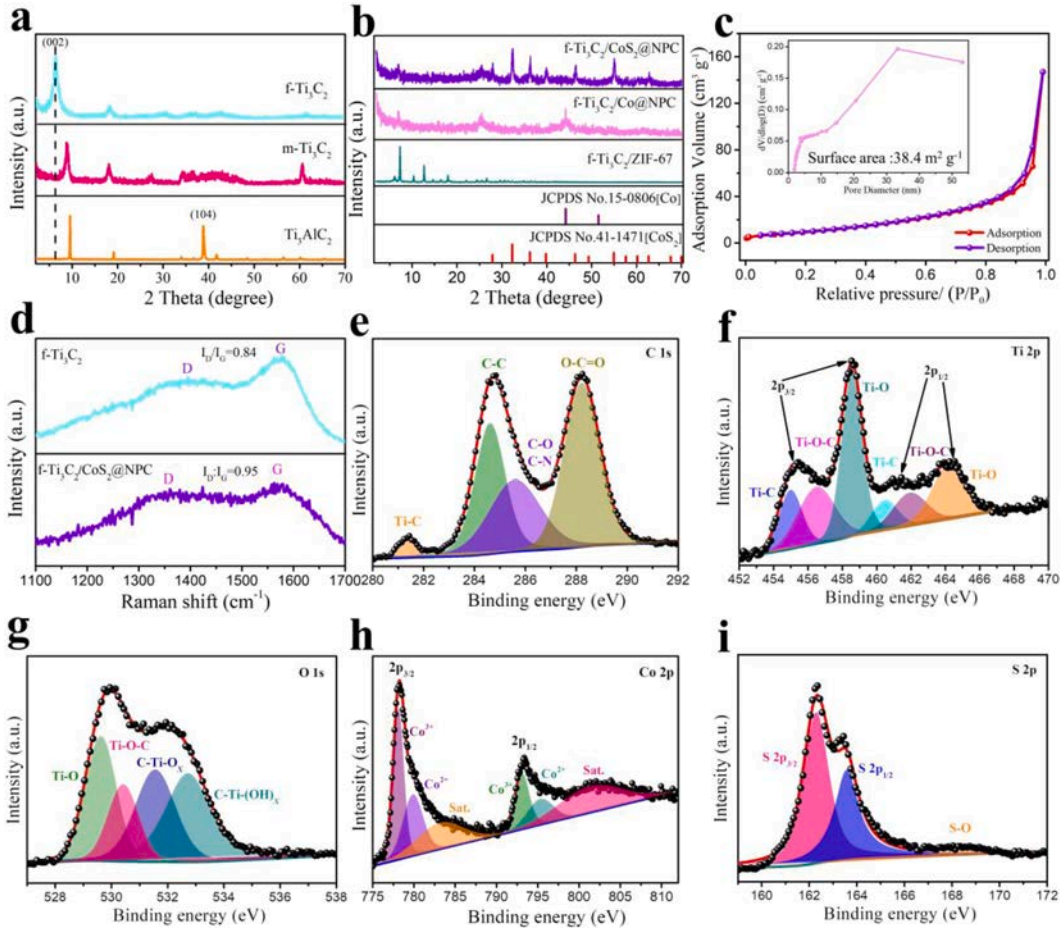

Fig. 2. (a) XRD patterns of Ti_3AlC_2, m-Ti_3C_2 and f-Ti_3C_2 MXene. (b) XRD patterns of Co standard spectrum, CoS_2 standard spectrum, f-Ti_3C_2/ZIF-67 hybrids, f-Ti_3C_2/Co@NPC composites and f-Ti_3C_2/CoS_2@NPC hybrids. (c) N_2 adsorption-desorption isotherm curve of f-Ti_3C_2/CoS_2@NPC hybrids, the inset corresponds to pore size distribution. (d) Raman spectrum of f-Ti_3C_2 MXene and f-Ti_3C_2/CoS_2@NPC hybrids. (e–i) C 1 s, Ti 2p, O 1 s, Co 2p and S 2p spectrum of f-Ti_3C_2/CoS_2@NPC hybrids.

high graphitization degree. However, the I_D/I_G ratio increases to 0.95 for f-Ti_3C_2/CoS_2@NPC hybrids, which is due to the existence of NPC layer with low graphitization degree. It can be calculated that the exact contents of f-Ti_3C_2, CoS_2 and NPC in f-Ti_3C_2/CoS_2@NPC composites are 35%, 50% and 15% (Fig. S2).

The X-ray photoelectron spectroscopy (XPS) is used to obtain the surface electronic state and chemical composition of CoS_2@NPC and f-Ti_3C_2/CoS_2@NPC hybrids. For CoS_2@NPC composites, the C-N bond in C 1 s spectrum (Fig. S3a) proves that porous carbon is doped by nitrogen element [43]. As shown in Fig. S4a, the Ti 2p, C 1 s, N 1 s, Co 2p and S 2p can be clearly observed in the full spectrum of f-Ti_3C_2/CoS_2@NPC hybrids, which suggests the integration among f-Ti_3C_2, CoS_2 and NPC. For f-Ti_3C_2/CoS_2@NPC composites, the C 1 s spectrum can be fitted into four peaks at binding energies of 281.3, 284.6, 285.6 and 288.2 eV (Fig. 2e), which correspond to Ti—C, C—C, C—O/C—N and O—C=O bonds [4,65], respectively. The emergence of Ti—C bond further confirms the presence of MXene. The N 1 s spectrum (Fig. S4b) comprises the pyridinic N (398.5 eV), pyrrolic N (399.5 eV), graphitic N (400.5 eV) and oxidized N (405.5 eV) [51,57,66]. The presence of pyridinic N can create enough defects and active sites, which is beneficial for the Na^+ migration [4,67]. The Ti 2p spectrum (Fig. 2f) exhibits six intense peaks, which are related to Ti-C $2p_{3/2}$ /Ti-C $2p_{1/2}$ (455.0/460.4 eV), Ti-O-C $2p_{3/2}$ /Ti-O-C $2p_{1/2}$ (456.5/461.9 eV) and Ti-O $2p_{3/2}$ /Ti-O $2p_{1/2}$ (458.6/464.2 eV) [68–69]. Meanwhile, the Ti—O—C bond at 530.4 eV can also be observed in the O 1 s spectrum (Fig. 2g) [70]. All these discussions demonstrate the existence of Ti—O—C bonds between Ti_3C_2 MXene and NPC layer, which is conducive to rapid charge transport and high structural stability [9,69]. In the Co 2p spectrum (Fig. 2h), six fitted peaks consist of Co^{3+} $2p_{3/2}$ /Co^{3+} $2p_{1/2}$ (778.2/793.2 eV) and Co^{2+} $2p_{3/2}$ /Co^{2+} $2p_{1/2}$ (779.9/795.4 eV) as well as two satellite peaks at 783.2/801.4 eV [62,71]. Furthermore, two peaks situated at 162.3, 163.5 eV belong to S $2p_{3/2}$ and S $2p_{1/2}$ orbitals in the S 2p spectrum (Fig. 2i), respectively, and the peak at 168.7 eV belongs to S—O bond [37]. All these results confirm the successful formation of f-Ti_3C_2/CoS_2@NPC hybrids.

The FESEM, TEM and HRTEM images of as-prepared materials are shown in Fig. 3 and Fig. S5–S8. Classical densely-packed structure of Ti_3AlC_2 and accordion-like layered structure of m-Ti_3C_2 MXene can be observed in Fig. S5 and Fig. 3a [17,49]. However, f-Ti_3C_2 MXene nanosheets display a highly puckered and obvious porous architecture without restacking phenomenon (Fig. 3b and Fig. S6a), demonstrating the feasibility of the SPF strategy [30]. Meanwhile, HRTEM images indicate that the number of f-Ti_3C_2 layers is about 8 and the interlayer distance is close to 1.35 nm (Fig. S6b). Pure ZIF-67 exhibits a uniform polyhedron structure with smooth surface, which becomes rough after heating process under Ar atmosphere (Fig. S7) [43,51]. Fig. 3c clearly reveals the distribution of polyhedral ZIF-67 on f-Ti_3C_2 nanosheets via an *in-situ* growth process. The SEM image of f-Ti_3C_2/CoS_2@NPC hybrids (Fig. 3d) indicates that Ti_3C_2 nanosheets are homogeneously decorated with CoS_2@NPC composites after the carbonization and sulfurization process. Furthermore, TEM and HRTEM images of CoS_2@NPC (Fig. 3e and Fig. S8) demonstrate that the CoS_2 NPs with a uniform size of 5–15 nm are embedded in an amorphous carbon matrix. Above discussions strongly confirm the preparation of MXene-supported CoS_2@NPC multidimensional hierarchical architecture. As shown in Fig. 3f, crystal plane with a *d*-spacing of 0.28 nm in HRTEM image corresponds to (200) plane of CoS_2 [72]. SEM elemental mapping images exhibited in Fig. 3g-k manifest that Ti, C, N, Co and S elements are uniformly distributed, further proving the successful loading of CoS_2@NPC on Ti_3C_2 MXene.

The sodium storage properties of as-prepared materials are first investigated by CV at a sweep rate of 0.1 mV s^{-1} in a potential range of 0.01–3 V (Fig. 4a and Fig. S9). In the initial cathodic scan, three peaks emerge at around 0.95, 0.66 and 0.46 V for f-Ti_3C_2/CoS_2@NPC hybrids

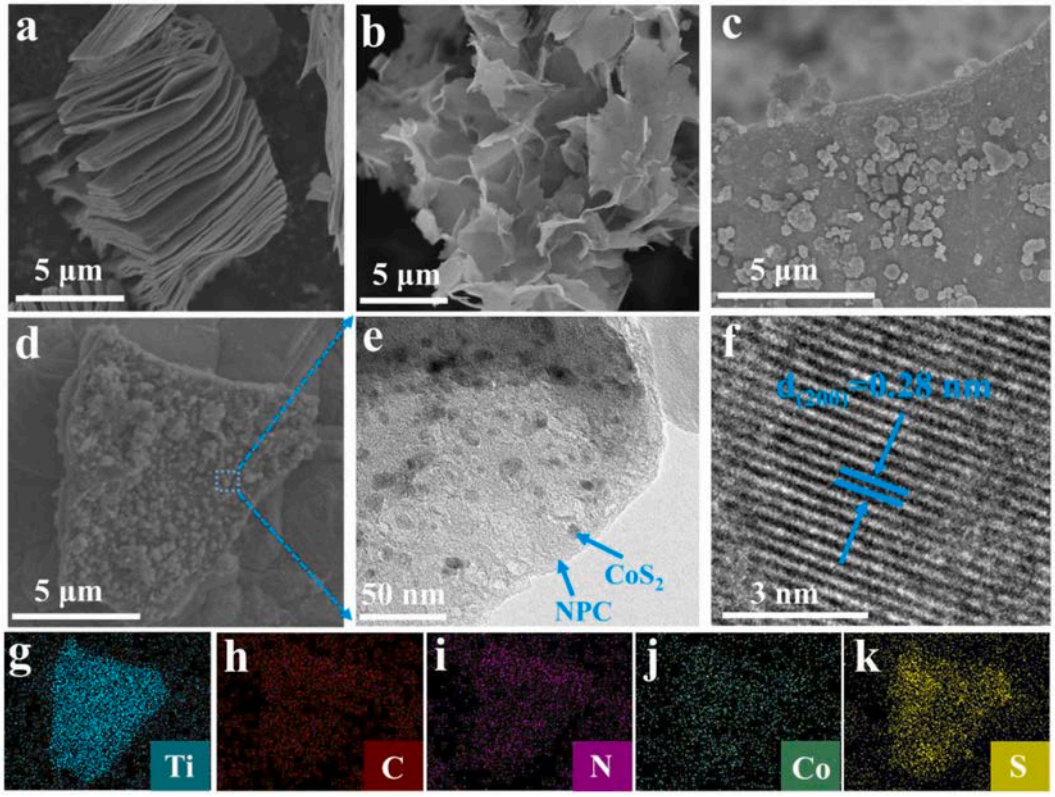

Fig. 3. (a) SEM image of m-Ti_3C_2 MXene. (b) SEM image of f-Ti_3C_2 MXene prepared by SPF strategy. (c) SEM image of f-Ti_3C_2/ZIF-67 hybrids. (d) SEM image of f-Ti_3C_2/CoS_2@NPC hybrids. (e) TEM image of selected rectangular area representing CoS_2@NPC hybrids. (f) HRTEM image of f-Ti_3C_2/CoS_2@NPC hybrids. (g–k) EDX element mappings of Ti, C, N, Co and S among f-Ti_3C_2/CoS_2@NPC composites.

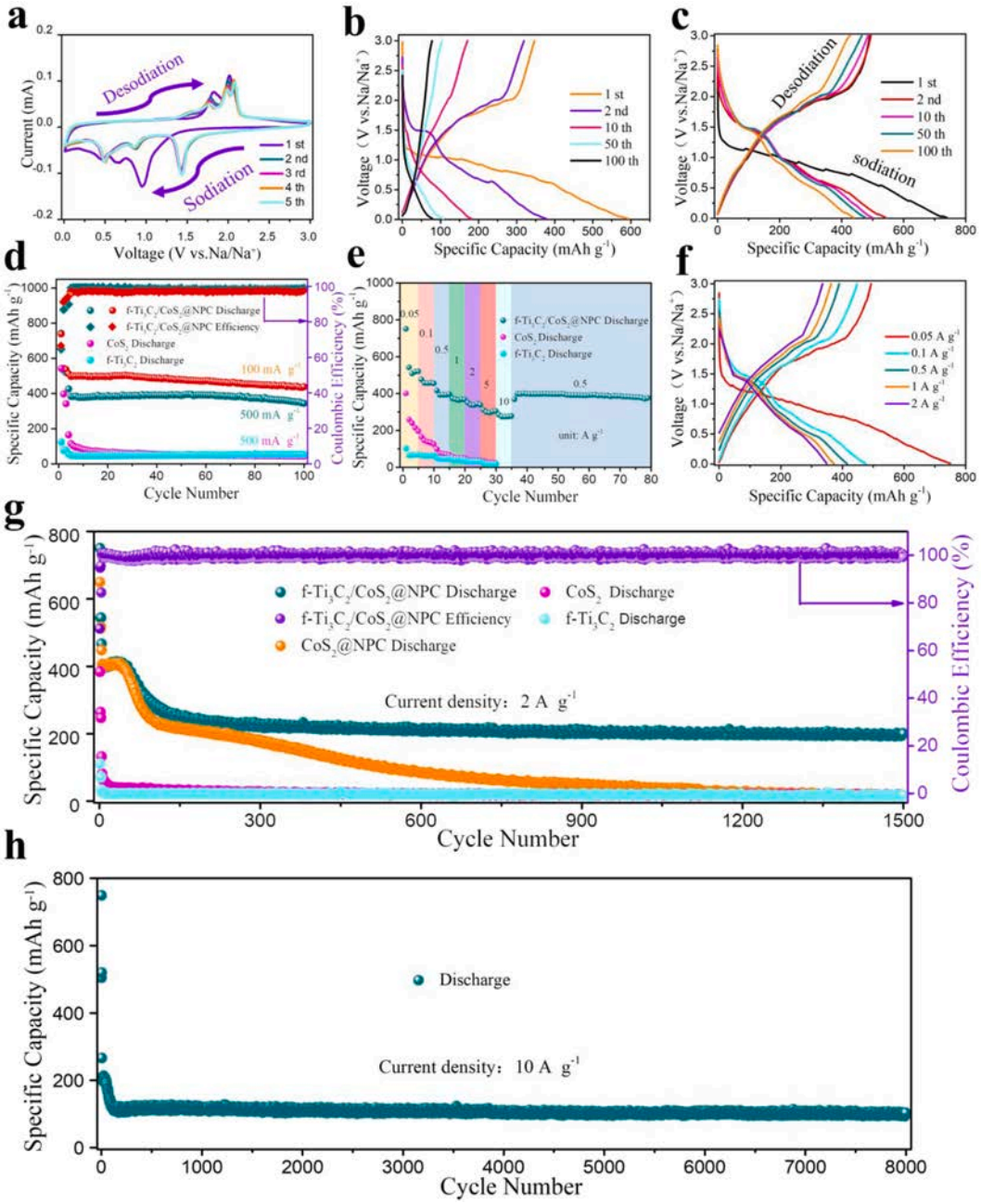

Fig. 4. (a) CV curve of f-Ti_3C_2/CoS_2@NPC electrode from 3.0 V to 0.01 V *vs* Na/Na^+ at a scan rate of 0.1 mV s^{-1}. (b-c) GCD curves of CoS_2 and f-Ti_3C_2/CoS_2@NPC anodes at 100 mA g^{-1}. (d) Cycling performance of different anodes at 100 mA g^{-1} and 500 mA g^{-1}. (e) Rate performance of different electrodes. (f) GCD profiles of f-Ti_3C_2/CoS_2@NPC electrode at different current densities. (g) Long cycling performance of different anodes at 2000 mA g^{-1}. (h) Ultralong cycling performance of f-Ti_3C_2/CoS_2@NPC electrode at 10 A g^{-1}.

(Fig. 4a). The peak at 0.95 V corresponds to the formation of Na_xCoS_2 and the peaks at about 0.66 and 0.46 V are originated from further sodiation process of Na_xCoS_2 to form Co and Na_2S [37,73]. Meanwhile, the peak at 0.66 V is also related to SEI layer generation [62,72]. Two anodic peaks at 1.83 and 2.02 V are associated with the decomposition of Na_2S and the formation of CoS_2 [71]. In the following cycles, the cathodic peaks at around 0.95, 0.66 and 0.46 V move to 1.43, 0.86 and 0.49 V, respectively, which is due to the electrochemical activation process and structural reorganization of electrode [36,56,58]. Additionally, initial anodic peak at 2.02 V turns into two peaks located at 2 and 2.06 V, which is in accordance with previously reported work [73]. It is noteworthy that CV curves coincide well in the following cycles, indicating exceptional cyclability and high reversibility of f-Ti_3C_2/CoS_2@NPC anode [8,74]. Meanwhile, a squarish CV curve can be observed for f-Ti_3C_2 MXene and broad peaks located at 0.96, 2.42 as well as 2.0 V can be ascribed to Na^+ extraction/insertion process (Fig. S9) [52,75], representing a typical pseudocapacitive reaction.

Fig. 4b, c and Fig. S10a demonstrate the GCD curves of f-Ti_3C_2 MXene, CoS_2 and f-Ti_3C_2/CoS_2@NPC composites at 100 mA g^{-1}. CoS_2 anode releases an initial discharge capacity of 594.0 mAh g^{-1} with a low initial coulombic efficiency (ICE) of 58.38% (Fig. 4b), which is mainly due to SEI film formation [62]. However, the discharge capacity sharply decreases to 79.3 mAh g^{-1} after 100 cycles and discharge/charge plateaus vanish simply after 10 cycles attributed to drastic volumetric expansion/shrinkage of CoS_2 during sodiation/desodiation process. The f-Ti_3C_2 MXene displays a low discharge capacity and typical

pseudocapacitive-shaped charge-discharge curves without plateau (Fig. S10a), which is conducive to rapid Na^+ transport [25]. The f-Ti_3C_2/CoS_2@NPC anode possesses an initial discharge capacity of 743.4 mAh g^{-1} and ICE of 64.6% (Fig. 4c), and the initial irreversible capacity can be assigned to the generation of SEI layer as well as the reactions between surface functional groups (−OH, −O and −F) of f-Ti_3C_2 MXene and Na^+ [71,76]. The slopy discharge plateau in the first cycle correlates with the sodiation process of f-Ti_3C_2/CoS_2@NPC electrode and SEI film creation. Additionally, the hybrids show obvious discharge plateaus located at around 1.47, 0.9 and 0.5 V as well as charge plateau situated at 1.8–2.1 V after 100 cycles, which is in good agreement with CV results and demonstrates outstanding structural stability.

The short-term cyclability of as-prepared materials at low current density is displayed in Fig. 4d and Fig. S10b, c. Pure CoS_2 and f-Ti_3C_2 anodes deliver a low specific capacity of 44.2 and 53.6 mAh g^{-1} after 100 cycles at 500 mA g^{-1} (Fig. 4d). For f-Ti_3C_2-550, it only exhibits a discharge capacity of 51.7 mAh g^{-1} at 500 mA g^{-1} after 500 cycles (Fig. S10b). In contrast, a high capacity of 438.4 and 344.3 mAh g^{-1} after 100 cycles can be obtained for f-Ti_3C_2/CoS_2@NPC hybrids at 100 and 500 mA g^{-1} (Fig. 4d), respectively. Additionally, CoS_2@NPC composites manifest low capacity decay rate within initial 70 cycles at 500 mA g^{-1} (Fig. S10c). The excellent short-term cyclability of CoS_2@NPC and f-Ti_3C_2/CoS_2@NPC anodes is mainly attributed to the protection effect of NPC layer and f-Ti_3C_2 MXene on CoS_2 NPs by alleviating the large volume change of CoS_2 NPs during Na^+ insertion/extraction process [6,24,41]. Fig. 4e and Fig. S10d, e reveal the rate performance of above-mentioned electrodes. Remarkably, f-Ti_3C_2/CoS_2@NPC composites retain a capacity of 749.7, 475, 414.2, 372.2, 348.7, 310.0 and 282.6 mAh g^{-1} at a current rate of 0.05, 0.1, 0.5, 1, 2 ,5 and 10 A g^{-1} (Fig. 4e), respectively, much better than f-Ti_3C_2, CoS_2 and f-Ti_3C_2-550, which release a low capacity of 23.5, 31.0 and 10.0 mAh g^{-1} at 5 A g^{-1} (Fig. 4e and Fig. S10d), respectively. Furthermore, a capacity of 396.9 mAh g^{-1} can be attained for f-Ti_3C_2/CoS_2@NPC hybrids when the current rate is returned to 0.5 A g^{-1}. Meanwhile, CoS_2@NPC composites also present enhanced rate performance owing to high electronic conductivity of NPC layer (Fig. S10e). The GCD profiles of f-Ti_3C_2/CoS_2@NPC composites at various current rates are depicted in Fig. 4f. Although voltage polarization gradually rises with the increase of current rate, the discharge and charge plateaus can be obviously observed even at 2 A g^{-1}. Nevertheless, the voltage plateaus of CoS_2 disappear at slightly high current densities and f-Ti_3C_2 MXene shows charge-discharge profiles without obvious redox plateau at various current densities (Fig. S11a, b). The outstanding rate capability can be assigned to the synergistic effect among f-Ti_3C_2 MXene with rapid Na^+/electron transport, CoS_2 NPs with high specific capacity and short Na^+ diffusion length as well as NPC layer with high electronic conductivity.

Fig. 4g-h compares the ultralong cyclability of different samples at high current rates. The f-Ti_3C_2, f-Ti_3C_2-550 and CoS_2 electrodes exhibit low specific capacities and mediocre cyclability (Fig. 4g and Fig. S11c, d). For CoS_2@NPC anode, the specific capacity remains stable without fading during the initial dozens of cycles and sharply decrease to around 15 mAh g^{-1} at various current densities after 1500 cycles (Fig. 4g and Fig. S12). The inferior cyclability is associated with the insufficient restraint ability of NPC coating layer, which cannot mitigate the massive volume variation of CoS_2 NPs during long-term cycling process, thereby engendering structural collapse and undesirable cyclability [42–44,74]. Contrastingly, f-Ti_3C_2/CoS_2@NPC anodes show robust long-term cyclic stability and deliver a high discharge capacity of 200.6 mAh g^{-1} at 2 A g^{-1} after 1500 cycles and 104.1 mAh g^{-1} at 10 A g^{-1} after 8000 cycles (Fig. 4g, h). The capacity fading after 50 cycles can be attributed to surface reconstruction of SEI film and CoS_2 NPs, which can be observed in other previous works. [7,58,77–80] The *ex-situ* SEM images of CoS_2@NPC and f-Ti_3C_2/CoS_2@NPC anodes after 8000 cycles are depicted in Fig. S13. Cracks can be obviously observed for CoS_2@NPC anode (Fig. S13a, b), which directly contributes to inferior cyclability. Nevertheless, f-Ti_3C_2/CoS_2@NPC electrode exhibits no cracks and maintain superior structural stability owing to the introduction of f-Ti_3C_2 MXene (Fig. S13c, d). The favorable ultralong cycle lifespan of f-Ti_3C_2/CoS_2@NPC electrode is superior to those of most previously reported works related to transition metal sulfide-based SIBs anodes (Table S1) [30,36–39]. Additionally, f-Ti_3C_2/CoS_2@NPC hybrids display a high and steady coulombic efficiency compared with CoS_2@NPC (Fig. S14a). The outstanding prolonged cyclic performance and stable coulombic efficiency further confirm the superiority of multidimensional synergistic architecture (Fig. 5).

In order to reveal the reason for remarkable sodium storage performance of f-Ti_3C_2/CoS_2@NPC hybrids, EIS is performed with an applied amplitude of 10 mV. The Nyquist plots of as-prepared electrodes consist of a compressed semicircle in the middle-to-high frequency region representing charge transfer resistance (R_{ct}) and a sloped line in the low frequency region reflecting Na^+ diffusion resistance within the electrodes before cycling [4,46,81] (Fig. 6a and Fig. S14b), which are simulated according to equivalent circuit (Fig. S15). Compared with f-Ti_3C_2, CoS_2 and CoS_2@NPC samples, f-Ti_3C_2/CoS_2@NPC composites possess the lowest R_{ct} value (Table S2). The R_{ct} value of f-Ti_3C_2/CoS_2@NPC hybrids gradually decreases upon cycling (Fig. 6b and Table S3), suggesting faster interfacial electron transport and robust structure. Additionally, f-Ti_3C_2/CoS_2@NPC anode shows a considerably lower R_{ct} value at 8000th cycle compared with CoS_2@NPC electrode (Fig. S16a and Table S4). The Bode plots of these materials are displayed in Fig. 6c, d and the value of phase angle at low frequency region (below 10^0 Hz) is in negative correlation with Na^+ diffusion ability in the electrode [58]. The f-Ti_3C_2/CoS_2@NPC anode demonstrates the smallest phase angle among different electrodes (Fig. 6c), exhibiting more advantageous Na^+ diffusion kinetics than CoS_2@NPC anode. Likewise, the phase angle value of f-Ti_3C_2/CoS_2@NPC hybrids reaches a minimum at 8000th cycle (Fig. 6d). Consequently, the introduction of f-Ti_3C_2 MXene can significantly facilitate the interfacial electron transport, strengthen Na^+ transport kinetics as well as maintain the structural integrity and stability of electrode based on above analysis [9,17,23], accordingly contributing to extraordinary rate performance and prolonged cycle life of f-Ti_3C_2/CoS_2@NPC composites.

To further explore the superior rate capability of f-Ti_3C_2/CoS_2@NPC anodes, CV profiles at different sweep rates are presented in Fig. 6e. The charge storage mechanism can be determined according to equation (1). [56]

$$i = av^b \tag{1}$$

where i stands for peak current, v is sweep rate, a and b are two adjustable parameters. Typically, $b = 0.5$ shows a diffusion-controlled process, while $b = 1$ indicates a capacitive-controlled process [8]. As exhibited in Fig. 6f, b-values are simulated to be 0.86, 0.86, 0.76, 0.90, 0.82 and 0.90 for peak 1, peak 2, peak 3, peak 4, peak 5 and peak 6 (Fig. S17), respectively. The large b-value manifests the coexistence of surface capacitive effect and diffusion-controlled process within the f-Ti_3C_2/CoS_2@NPC electrodes. Furthermore, Nyquist plot of f-Ti_3C_2/CoS_2@NPC electrode at 8000th cycle (Fig. 6g) shows that the angle between inclined line and Z′-axis is around 75.8° and n-value of 0.84 can be attained based on equivalent circuit model (Fig. S18, 19). Similarly, a large n-value can also prove that surface capacitive process dominates the sodium storage mechanism [5,82]. In contrast, CoS_2@NPC composites possess typical diffusion-controlled electrochemical behavior (Fig. S16a). The capacitive contribution can be quantified by eq. (2) [3].

$$i = k_1 v + k_2 v^{1/2} \tag{2}$$

where k_1v and $k_2v^{1/2}$ suggest surface capacitive contribution and diffusion-controlled process contribution [72], respectively. As demonstrated in Fig. 6h, capacitive contribution reaches 92.8% at 0.5 mV/s. Additionally, the capacitive contribution gradually rises with increasing sweep rates and can achieve 97.1% at 1.0 mV/s (Fig. 6i). Such a high capacitive contribution is conducive to ultrafast Na^+ transport

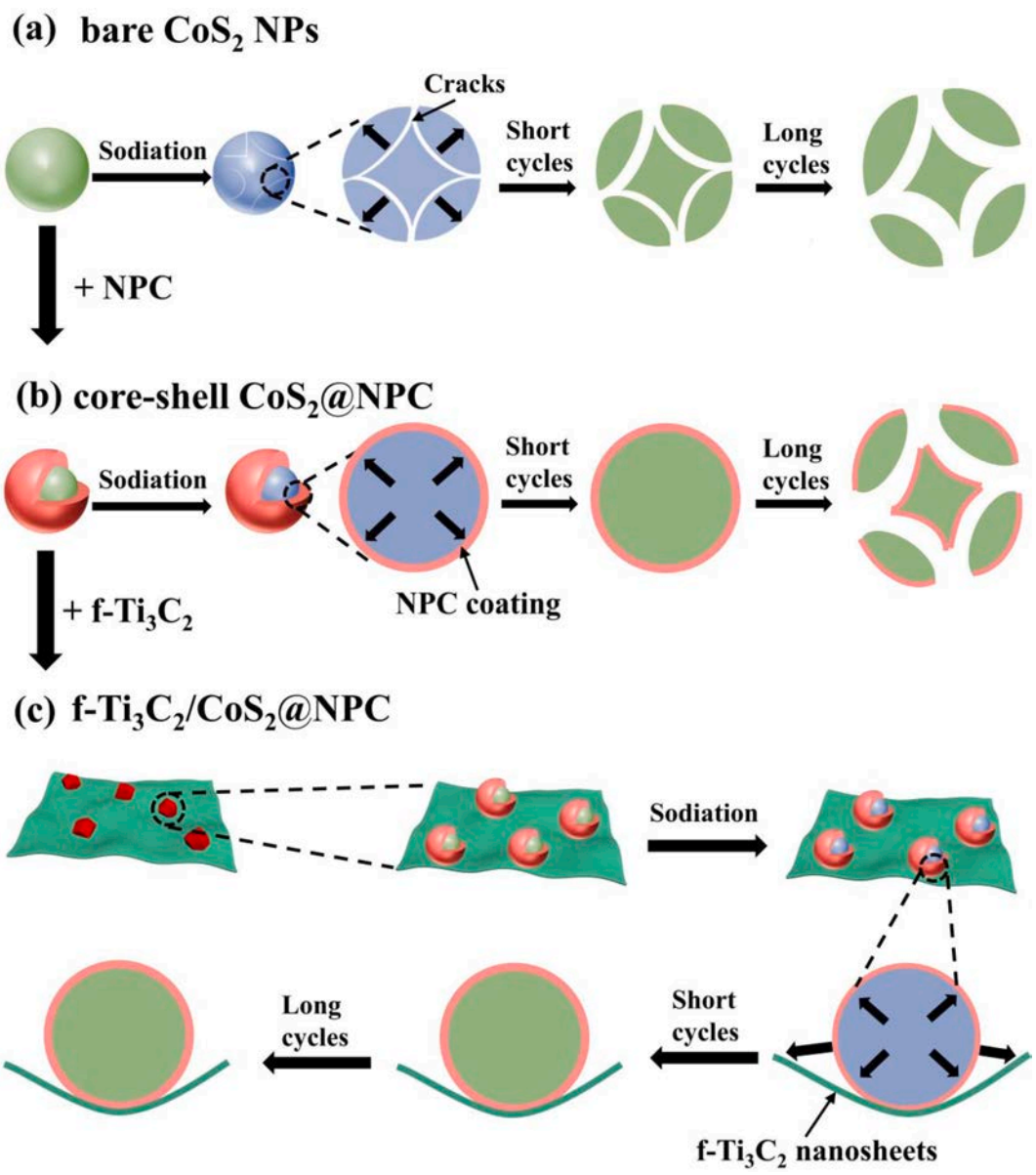

Fig. 5. Schematic illustration of the electrochemical process for three electrodes with different configurations. (a) bare CoS_2 NPs. (b) CoS_2@NPC hybrids. (c) f-Ti_3C_2/CoS_2@NPC composites.

[25,56,67,82], therefore rendering excellent rate performance when combined with impressive electronic conductivity of f-Ti_3C_2 MXene and NPC layer [24].

Galvanostatic intermittent titration technique (GITT) test is performed at 50 mA g^{-1} to further evaluate Na^+ diffusion kinetics of f-Ti_3C_2, CoS_2, CoS_2@NPC and f-Ti_3C_2/CoS_2@NPC anodes. As shown in Fig. 6j, compared with another three electrodes, f-Ti_3C_2/CoS_2@NPC anodes demonstrate the smallest overvoltage and longest charge-discharge time, suggesting the lowest resistance of Na^+ diffusion [47]. The Na^+ diffusion coefficient (D_{Na}) can be obtained by eq. (3)

$$D_{Na} = \frac{4}{\pi\tau}\left(\frac{mV_m}{MA}\right)^2\left(\frac{\Delta E_s}{\Delta E_\tau}\right)^2 \quad (3)$$

where τ refers to the current pulse duration, m stands for the mass of active materials, A means the geometric area of electrode. V_m and M denote the molar volume and molar mass of active materials, respectively [9]. The calculation results are presented in Fig. 6k and Fig. S20. The D_{Na} of f-Ti_3C_2 and f-Ti_3C_2/CoS_2@NPC electrodes are in the order of 10^{-10}–10^{-14} and 10^{-11}–10^{-13} cm^2 s^{-1}, respectively, much higher than that of CoS_2 (10^{-11}–10^{-15} cm^2 s^{-1}). Based on above discussion, it can be concluded that f-Ti_3C_2/CoS_2@NPC hybrids greatly accelerate Na^+/electron transport during sodiation/desodiation process, owing to the introduction of f-Ti_3C_2 MXene and NPC layer (Fig. 7a), therefore leading to outstanding rate capability.

Encouraged by the superior electrochemical performance of the Na// Ti_3C_2/CoS_2@NPC half-cell, we decide to assemble full cell to explore its practical application (Fig. 7b). Owing to high Na^+ conductivity and high voltage plateau, $Na_3V_2(PO_4)_3$ (NVP) is considered as a suitable cathode for SIBs [12,67]. Therefore, NVP is selected as cathode to couple with f-Ti_3C_2/CoS_2@NPC anode. The XRD diffraction pattern of NVP indicates high phase purity and the SEM images reveal that NVP consists of microspheres (Fig. S21). When investigated in half cells within the voltage range of 2.0–4.3 V, NVP cathode displays a flat discharge/charge plateau at around 3.4 V and releases a reversible specific capacity of 95.6 mAh g^{-1} at 200 mA g^{-1} after 200 cycles (Fig. S22). As shown in Fig. 7c, the coin-type NVP//f-Ti_3C_2/CoS_2@NPC full cell can simultaneously light up two or three light-emitting diodes (LEDs). The GCD

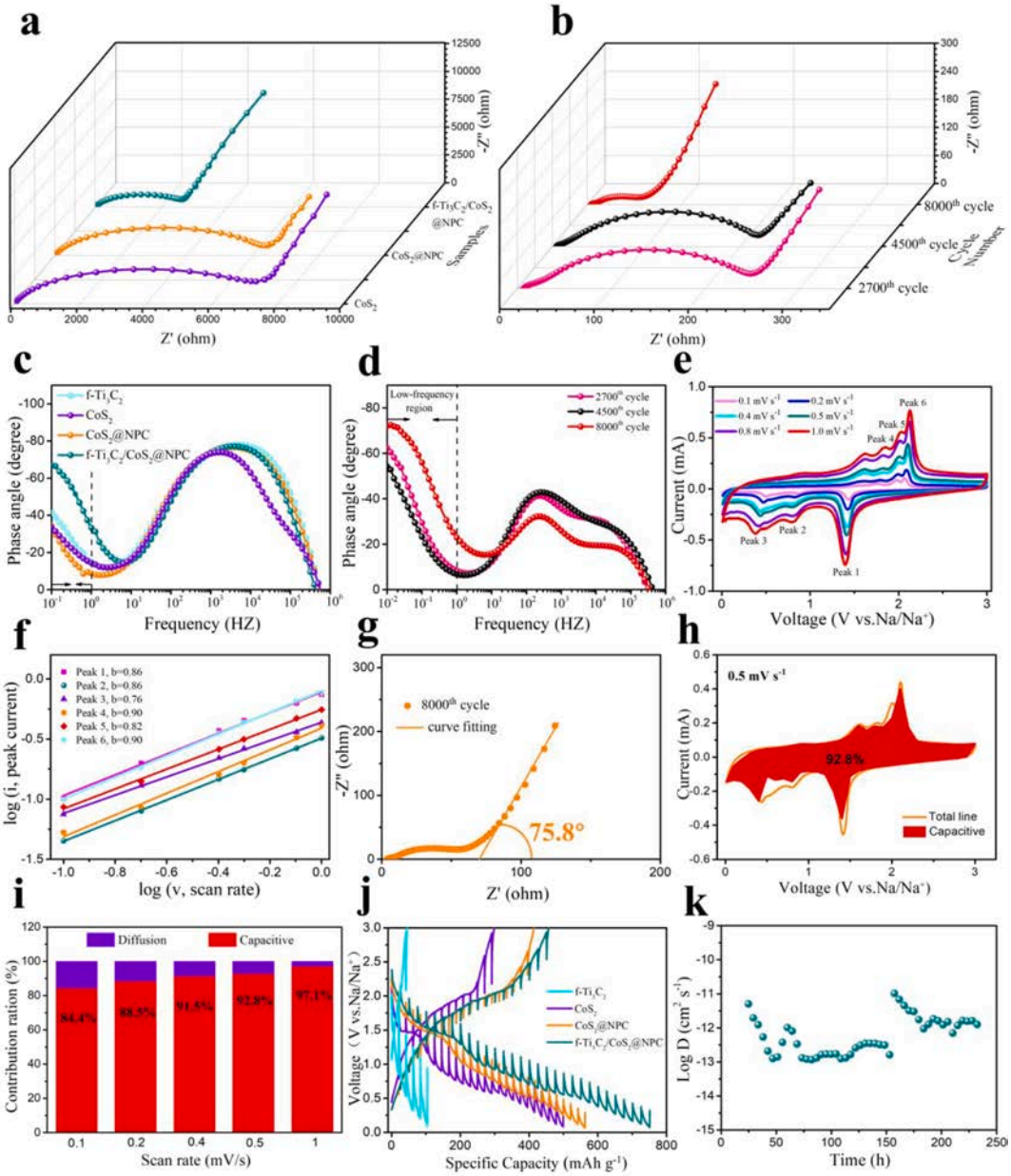

Fig. 6. (a) Nyquist plots of the CoS_2, CoS_2@NPC and f-Ti_3C_2/CoS_2@NPC anodes before cycling. (b) Nyquist plots of f-Ti_3C_2/CoS_2@NPC electrode after 2700, 4500 and 8000 cycles. (c) Bode plots of f-Ti_3C_2, CoS_2, CoS_2@NPC and f-Ti_3C_2/CoS_2@NPC electrodes before cycling. (d) Bode plots of f-Ti_3C_2/CoS_2@NPC electrode after 2700, 4500 and 8000 cycles. (e) CV curves of the f-Ti_3C_2/CoS_2@NPC anode at different sweep rates. (f) The plots of log (i) *vs* log (v) calculated from CV curves. (g) Nyquist plot of f-Ti_3C_2/CoS_2@NPC anode at 8000th cycle. (h) CV curve with corresponding capacitive contribution at 0.5 mV s^{-1}. (i) Capacitive contribution at different sweep rates. (j) The GITT curves of different electrodes (current density at 50 mA g^{-1}). (k) Na^+ diffusion coefficient of f-Ti_3C_2/CoS_2@NPC electrode during the charge-discharge process.

curves between 0.4 and 3.4 V at 200 mA g^{-1} (Fig. 7d) suggest that the full cell presents an initial discharge capacity of 454.1 mAh g^{-1} (calculated by the anode mass) with an output voltage of 2.1 V and the ICE can reach 87.7%. Furthermore, the full cell demonstrates a discharge capacity of 325.8 mAh g^{-1} after 50 cycles at 200 mA g^{-1} (Fig. 7e). These discussions indicate that f-Ti_3C_2/CoS_2@NPC anode has potential application prospect. The sodiation performance of full cell can be further improved by pairing f-Ti_3C_2/CoS_2@NPC anode with other cathode materials, changing electrolyte and optimizing the mass ratio of cathode to anode.

4. Conclusions

In summary, f-Ti_3C_2/CoS_2@NPC hybrids with multidimensional synergistic structure have been successfully prepared as SIBs anodes by carbonization and sulfurization treatment of f-Ti_3C_2/ZIF-67 composites. Within the hierarchical structure, the electronic conductivity can be greatly improved by the introduction of f-Ti_3C_2 MXene and NPC coating layer and a rapid Na^+ ion conductive network can be provided by f-Ti_3C_2 MXene. Additionally, f-Ti_3C_2 MXene can stop NPC layer from cracking induced by huge volume change of CoS_2 NPs during Na^+ insertion/extraction process via Ti—O—C covalent bonding, therefore leading to a dual protection effect on CoS_2 NPs. Each component makes full use of its own strength and overcomes the disadvantages of other units. The synergy among each unit endows the f-Ti_3C_2/CoS_2@NPC anode with superior charge transfer kinetics and high structural integrity, leading to superior rate capability and ultralong cycle lifespan (104.1 mAh g^{-1} at 10 A g^{-1} after 8000 cycles). Furthermore, the NVP//f-Ti_3C_2/CoS_2@NPC

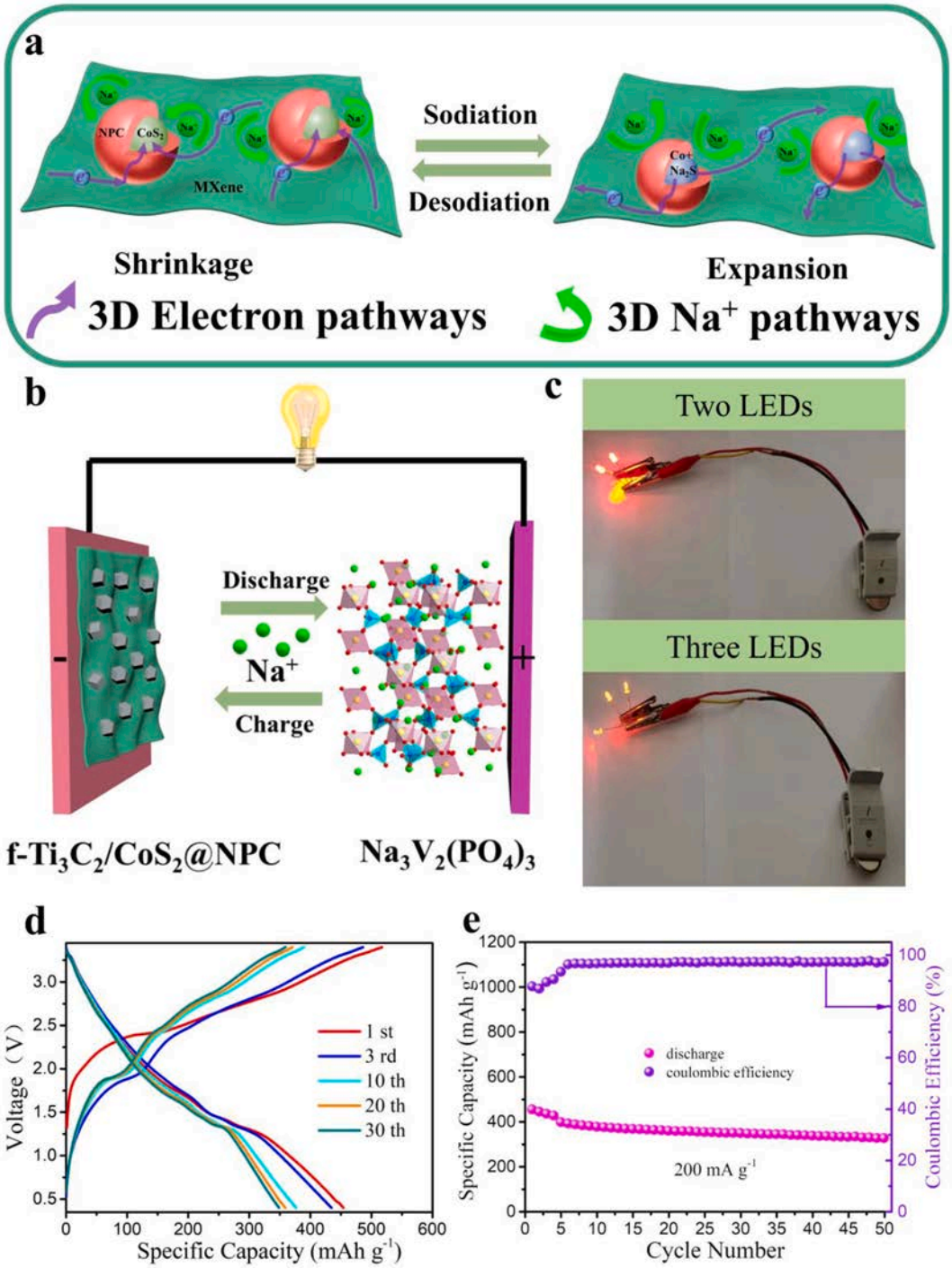

Fig. 7. (a) Schematic illustration showing the sodiation/desodiation mechanism of f-Ti_3C_2/CoS_2@NPC hybrids. (b) Schematic illustration of $Na_3V_2(PO_4)_3$//f-Ti_3C_2/CoS_2@NPC full cell. (c) Digital pictures of lighted LEDs driven by the coin-type full cell. (d) GCD curves of full cell at 200 mA g^{-1}. (e) Cycling performance of full cell at 200 mA g^{-1}.

full cell possesses good cyclability (325.8 mAh g^{-1} at 200 mA g^{-1} after 50 cycles). This work proposes a simple strategy to design multidimensional synergistic architecture, which can be readily applied to prepare other MXene-based hierarchical structure as SIBs anodes with superior electrochemical performance.

Declaration of Competing Interest

The authors declare that they have no known competing financial interests or personal relationships that could have appeared to influence the work reported in this paper.

Acknowledgements

This work was supported by the fund from National Natural Science Foundation of China (51901206), Taihu Electric Corporation 0001 and "the Fundamental Research Funds for the Central Universities" (2021QNA4003)

Appendix A. Supplementary data

Supplementary data to this article can be found online at https://doi.org/10.1016/j.cej.2021.132396.

References

[1] S. Sun, C. Liao, A.M. Hafez, H. Zhu, S. Wu, Two-dimensional MXenes for energy storage, Chem. Eng. J. 338 (2018) 27–45.
[2] T.M. Gür, Review of electrical energy storage technologies, materials and systems: challenges and prospects for large-scale grid storage, Energy Environ. Sci. 11 (2018) 2696–2767.
[3] X. Wang, Y. Li, S. Wang, F. Zhou, P. Das, C. Sun, S. Zheng, Z.S. Wu, 2D amorphous V_2O_5/graphene heterostructures for high-safety aqueous Zn-ion batteries with unprecedented capacity and ultrahigh rate capability, Adv. Energy Mater. 10 (2020) 2000081.
[4] R. Zhao, H. Di, X. Hui, D. Zhao, R. Wang, C. Wang, L. Yin, Self-assembled Ti_3C_2 MXene and N-rich porous carbon hybrids as superior anodes for high-performance potassium-ion batteries, Energy Environ. Sci. 13 (2020) 246–257.
[5] H. Lin, M. Li, X. Yang, D. Yu, Y. Zeng, C. Wang, G. Chen, F. Du, Nanosheets-assembled CuSe crystal pillar as a stable and high-power anode for sodium-ion and potassium-ion batteries, Adv. Energy Mater. 9 (2019) 1900323.
[6] Y. Dong, H. Shi, Z.S. Wu, Recent advances and promise of MXene-based nanostructures for high-performance metal ion batteries, Adv. Funct. Mater. 30 (2020) 2000706.
[7] D. Zhao, R. Zhao, S. Dong, X. Miao, Z. Zhang, C. Wang, L. Yin, Alkali-induced 3D crinkled porous Ti_3C_2 MXene architectures coupled with NiCoP bimetallic phosphide nanoparticles as anodes for high-performance sodium-ion batteries, Energy Environ. Sci. 12 (2019) 2422–2432.
[8] Y. Ding, Y. Chen, N. Xu, X. Lian, L. Li, Y. Hu, S. Peng, Facile synthesis of $FePS_3$ nanosheets@MXene composite as a high-performance anode material for sodium storage, Nano-Micro Lett. 12 (2020) 54.
[9] E. Xu, Y. Zhang, H. Wang, Z. Zhu, J. Quan, Y. Chang, P. Li, D. Yu, Y. Jiang, Ultrafast kinetics net electrode assembled via $MoSe_2$/MXene heterojunction for high-performance sodium-ion batteries, Chem. Eng. J. 385 (2020), 123839.
[10] X.L. Huang, Y.-X. Wang, S.-L. Chou, S.X. Dou, Z.M. Wang, Materials engineering for adsorption and catalysis in room-temperature Na-S batteries, Energy Environ. Sci. 14 (2021) 3757–3795.
[11] M. Luo, H. Yu, F. Hu, T. Liu, X. Cheng, R. Zheng, Y. Bai, M. Shui, J. Shu, Metal selenides for high performance sodium ion batteries, Chem. Eng. J. 380 (2020), 122557.
[12] J.-Y. Hwang, S.-T. Myung, Y.-K. Sun, Sodium-ion batteries: present and future, Chem. Soc. Rev. 46 (2017) 3529–3614.
[13] I. Hasa, J. Hassoun, S. Passerini, Nanostructured Na-ion and Li-ion anodes for battery application: a comparative overview, Nano Res. 10 (2017) 3942–3969.
[14] M. Naguib, M. Kurtoglu, V. Presser, J. Lu, J. Niu, M. Heon, L. Hultman, Y. Gogotsi, M.W. Barsoum, Two-dimensional nanocrystals produced by exfoliation of Ti_3AlC_2, Adv. Mater. 23 (2011) 4248–4253.
[15] R. Fang, C. Lu, A. Chen, K. Wang, H. Huang, Y. Gan, C. Liang, J. Zhang, X. Tao, Y. Xia, W. Zhang, 2D MXene-based energy storage materials: interfacial structure design and functionalization, ChemSusChem 13 (2020) 1409–1419.
[16] Y. Li, H. Shao, Z. Lin, J. Lu, L. Liu, B. Duployer, P.O.Å. Persson, P. Eklund, L. Hultman, M. Li, K.e. Chen, X.-H. Zha, S. Du, P. Rozier, Z. Chai, E. Raymundo-Piñero, P.-L. Taberna, P. Simon, Q. Huang, A general lewis acidic etching route for preparing MXenes with enhanced electrochemical performance in non-aqueous electrolyte, Nat. Mater. 19 (2020) 894–899.
[17] J. Pang, R.G. Mendes, A. Bachmatiuk, L. Zhao, H.Q. Ta, T. Gemming, H. Liu, Z. Liu, M.H. Rummeli, Applications of 2D MXenes in energy conversion and storage systems, Chem. Soc. Rev. 48 (2019) 72–133.
[18] J. Zhang, Y. Zhao, X. Guo, C. Chen, C.-L. Dong, R.-S. Liu, C.-P. Han, Y. Li, Y. Gogotsi, G. Wang, Single platinum atoms immobilized on an MXene as an efficient catalyst for the hydrogen evolution reaction, Nat. Catal. 1 (2018) 985–992.
[19] Y.-J. Wan, K. Rajavel, X.-M. Li, X.-Y. Wang, S.-Y. Liao, Z.-Q. Lin, P.-L. Zhu, R. Sun, C.-P. Wong, Electromagnetic interference shielding of $Ti_3C_2T_x$ MXene modified by ionic liquid for high chemical stability and excellent mechanical strength, Chem. Eng. J. 408 (2021), 127303.
[20] B.-M. Jun, S. Kim, J. Heo, C.M. Park, N. Her, M. Jang, Y.i. Huang, J. Han, Y. Yoon, Review of MXenes as new nanomaterials for energy storage/delivery and selected environmental applications, Nano Res. 12 (2018) 471–487.
[21] S. Han, Y.u. Chen, Y. Hao, Y. Xie, D. Xie, Y. Chen, Y. Xiong, Z. He, F. Hu, L. Li, J. Zhu, S. Peng, Multi-dimensional hierarchical CoS2@MXene as trifunctional electrocatalysts for zinc-air batteries and overall water splitting, Sci. China Mater. 64 (2021) 1127–1138.
[22] Z. Hu, Y. Xie, D. Yu, Q. Liu, L. Zhou, K. Zhang, P. Li, F. Hu, L. Li, S. Chou, S. Peng, Hierarchical $Ti_3C_2T_x$ MXene/carbon nanotubes for low overpotential and long-life Li-CO_2 batteries, ACS Nano 15 (2021) 8407–8417.
[23] S. Zhang, W.-Q. Han, Recent advances in MXenes and their composites in lithium/sodium batteries from the viewpoints of components and interlayer engineering, Phys. Chem. Chem. Phys. 22 (2020) 16482–16526.
[24] Y. Wu, Y. Yu, 2D material as anode for sodium ion batteries: recent progress and perspectives, Energy Storage Mater. 16 (2019) 323–343.
[25] X. Xie, K. Kretschmer, B. Anasori, B. Sun, G. Wang, Y. Gogotsi, Porous $Ti_3C_2T_x$ MXene for ultrahigh-rate sodium-ion storage with long cycle life, ACS Appl. Nano Mater. 1 (2018) 505–511.
[26] X. Song, H. Wang, S. Jin, M. Lv, Y. Zhang, X. Kong, H. Xu, T. Ma, X. Luo, H. Tan, D. Hu, C. Deng, X. Chang, J. Xu, Oligolayered $Ti_3C_2T_x$ MXene towards high performance lithium/sodium storage, Nano Res. 13 (2020) 1659–1667.
[27] Y.Z. Fang, R. Hu, K. Zhu, K. Ye, J. Yan, G. Wang, D. Cao, Aggregation-resistant 3D $Ti_3C_2T_x$ MXene with enhanced kinetics for potassium ion hybrid capacitors, Adv. Funct. Mater. 30 (2020) 2005663.
[28] J. Li, X. Yuan, C. Lin, Y. Yang, L. Xu, X. Du, J. Xie, J. Lin, J. Sun, Achieving high pseudocapacitance of 2D titanium carbide (MXene) by cation intercalation and surface modification, Adv. Energy Mater. 7 (2017) 1602725.
[29] Y.-J. Lei, Z.-C. Yan, W.-H. Lai, S.-L. Chou, Y.-X. Wang, H.-K. Liu, S.-X. Dou, Tailoring MXene-based materials for sodium-ion storage: synthesis, mechanisms, and applications, Electrochem. Energy Rev. 3 (2020) 766–792.
[30] D. Zhao, M. Clites, G. Ying, S. Kota, J. Wang, V. Natu, X. Wang, E. Pomerantseva, M. Cao, M.W. Barsoum, Alkali-induced crumpling of $Ti_3C_2T_x$ (MXene) to form 3D porous networks for sodium ion storage, Chem. Commun. 54 (2018) 4533–4536.
[31] V. Natu, M. Clites, E. Pomerantseva, M.W. Barsoum, Mesoporous MXene powders synthesized by acid induced crumpling and their use as Na-ion battery anodes, Mater. Res. Lett. 6 (2018) 230–235.
[32] K. Li, M. Liang, H. Wang, X. Wang, Y. Huang, J. Coelho, S. Pinilla, Y. Zhang, F. Qi, V. Nicolosi, Y. Xu, 3D MXene architectures for efficient energy storage and conversion, Adv. Funct. Mater. 30 (2020) 2000842.
[33] D. Er, J. Li, M. Naguib, Y. Gogotsi, V.B. Shenoy, Ti_3C_2 MXene as a high capacity electrode material for metal (Li, Na, K, Ca) ion batteries, ACS Appl. Mater. Interfaces 6 (2014) 11173–11179.
[34] B. Anasori, M.R. Lukatskaya, Y. Gogotsi, 2D metal carbides and nitrides (MXenes) for energy storage, Nat. Rev. Mater. 2 (2017) 16098.
[35] Y.V. Lim, X.L. Li, H.Y. Yang, Recent Tactics and advances in the application of metal sulfides as high-performance anode materials for rechargeable sodium-ion batteries, Adv. Funct. Mater. 31 (2021) 2006761.
[36] Y. Ma, Y. Ma, D. Bresser, Y. Ji, D. Geiger, U. Kaiser, C. Streb, A. Varzi, S. Passerini, Cobalt disulfide nanoparticles embedded in porous carbonaceous micro-polyhedrons interlinked by carbon nanotubes for superior lithium and sodium storage, ACS Nano 12 (2018) 7220–7231.
[37] W. Zhang, Z. Yue, Q. Wang, X. Zeng, C. Fu, Q. Li, X. Li, L. Fang, L. Li, Carbon-encapsulated CoS_2 nanoparticles anchored on N-doped carbon nanofibers derived from ZIF-8/ZIF-67 as anode for sodium-ion batteries, Chem. Eng. J. 380 (2020), 122548.
[38] Y. Zhang, N. Wang, C. Sun, Z. Lu, P. Xue, B. Tang, Z. Bai, S. Dou, 3D spongy CoS_2 nanoparticles/carbon composite as high-performance anode material for lithium/sodium ion batteries, Chem. Eng. J. 332 (2018) 370–376.
[39] Y. Pan, X. Cheng, Y. Huang, L. Gong, H. Zhang, CoS_2 Nanoparticles wrapping on flexible freestanding multichannel carbon nanofibers with high performance for Na-ion batteries, ACS Appl. Mater. Interfaces 9 (2017) 35820–35828.
[40] W. Sun, X. Tang, Y. Wang, Multi-metal-organic frameworks and their derived materials for Li/Na-ion batteries, Electrochem. Energy Rev. 3 (2020) 127–154.
[41] Z. Zhang, Y. Huang, X. Gao, Z. Xu, X. Wang, Rational design of hierarchically structured CoS_2@NCNTs from metal-organic frameworks for efficient lithium/sodium storage performance, ACS Appl. Energy Mater. 3 (2020) 6205–6214.
[42] S. Wang, P. Xiong, X. Guo, J. Zhang, X. Gao, F. Zhang, X. Tang, P.H.L. Notten, G. Wang, A stable conversion and alloying anode for potassium-ion batteries: a combined strategy of encapsulation and confinement, Adv. Funct. Mater. 30 (2020) 2001588.
[43] B. Zhao, Q. Liu, G. Wei, J. Wang, X.-Y. Yu, X. Li, H.B. Wu, Synthesis of $CoSe_2$ nanoparticles embedded in N-doped carbon with conformal TiO_2 shell for sodium-ion batteries, Chem. Eng. J. 378 (2019), 122206.
[44] Z. Chen, R. Wu, M. Liu, H. Wang, H. Xu, Y. Guo, Y. Song, F. Fang, X. Yu, D. Sun, General synthesis of dual carbon-confined metal sulfides quantum dots toward high-performance anodes for sodium-ion batteries, Adv. Funct. Mater. 27 (2017) 1702046.
[45] S. Tan, Y. Jiang, Q. Wei, Q. Huang, Y. Dai, F. Xiong, Q. Li, Q. An, X. Xu, Z. Zhu, X. Bai, L. Mai, Multidimensional synergistic nanoarchitecture exhibiting highly stable and ultrafast sodium-ion storage, Adv. Mater. 30 (2018) 1707122.
[46] Y. Wang, Y. Li, Z. Qiu, X. Wu, P. Zhou, T. Zhou, J. Zhao, Z. Miao, J. Zhou, S. Zhuo, Fe_3O_4@Ti_3C_2 MXene hybrids with ultrahigh volumetric capacity as an anode material for lithium-ion batteries, J. Mater. Chem. A 6 (2018) 11189–11197.
[47] X. Li, M. Li, Q. Yang, D. Wang, L. Ma, G. Liang, Z. Huang, B. Dong, Q. Huang, C. Zhi, Vertically aligned Sn^{4+} preintercalated Ti_2CT_X MXene sphere with enhanced Zn ion transportation and superior cycle lifespan, Adv. Energy Mater. 10 (2020) 2001394.
[48] Q. Zhao, Q. Zhu, J. Miao, P. Zhang, P. Wan, L. He, B. Xu, Flexible 3D porous MXene foam for high-performance lithium-ion batteries, Small 15 (2019) 1904293.
[49] S. Zhang, P. Huang, J. Wang, Z. Zhuang, Z. Zhang, W.Q. Han, Fast and universal solution-phase flocculation strategy for scalable synthesis of various few-layered mxene powders, J. Phys. Chem. Lett. 11 (2020) 1247–1254.
[50] P. Huang, S. Zhang, H. Ying, W. Yang, J. Wang, R. Guo, W. Han, Fabrication of Fe nanocomplex pillared few-layered $Ti_3C_2T_x$ MXene with enhanced rate performance for lithium-ion batteries, Nano Res. 14 (2021) 1218–1227.
[51] Y. Xie, J. Hu, Z. Han, T. Wang, J. Zheng, L. Gan, Y. Lai, Z. Zhang, Encapsulating sodium deposition into carbon rhombic dodecahedron guided by sodiophilic sites for dendrite-free na metal batteries, Energy Storage Mater. 30 (2020) 1–8.
[52] J. Li, D. Yan, S. Hou, Y. Li, T. Lu, Y. Yao, L. Pan, Improved sodium-ion storage performance of $Ti_3C_2T_x$ MXenes by sulfur doping, J. Mater. Chem. A 6 (2018) 1234–1243.

[53] J. Luo, W. Zhang, H. Yuan, C. Jin, L. Zhang, H. Huang, C. Liang, Y. Xia, J. Zhang, Y. Gan, X. Tao, Pillared structure design of MXene with ultralarge interlayer spacing for high-performance lithium-ion capacitors, ACS Nano 11 (2017) 2459–2469.
[54] M. Alhabeb, K. Maleski, B. Anasori, P. Lelyukh, L. Clark, S. Sin, Y. Gogotsi, Guidelines for synthesis and processing of two-dimensional titanium carbide ($Ti_3C_2T_x$ MXene), Chem. Mater. 29 (2017) 7633–7644.
[55] M. Ghidiu, J. Halim, S. Kota, D. Bish, Y. Gogotsi, M.W. Barsoum, Ion-exchange and cation solvation reactions in Ti_3C_2 MXene, Chem. Mater. 28 (2016) 3507–3514.
[56] J. Yang, H. Gao, S. Men, Z. Shi, Z. Lin, X. Kang, S. Chen, $CoSe_2$ Nanoparticles encapsulated by N-Doped carbon framework intertwined with carbon nanotubes: high-performance dual-role anode materials for both Li- and Na-ion batteries, Adv. Sci. 5 (2018) 1800763.
[57] S. Liu, J. Li, X. Yan, Q. Su, Y. Lu, J. Qiu, Z. Wang, X. Lin, J. Huang, R. Liu, B. Zheng, L. Chen, R. Fu, D. Wu, Superhierarchical cobalt-embedded nitrogen-doped porous carbon nanosheets as two-in-one hosts for high-performance lithium-sulfur batteries, Adv. Mater. 30 (2018) 1706895.
[58] R. Zhao, H. Di, C. Wang, X. Hui, D. Zhao, R. Wang, L. Zhang, L. Yin, Encapsulating ultrafine Sb nanoparticles in Na^+ pre-intercalated 3D porous $Ti_3C_2T_x$ MXene nanostructures for enhanced potassium storage performance, ACS Nano 14 (2020) 13938–13951.
[59] Q.i. Yang, Z. Huang, X. Li, Z. Liu, H. Li, G. Liang, D. Wang, Q. Huang, S. Zhang, S. Chen, C. Zhi, A wholly degradable, rechargeable Zn-Ti_3C_2 MXene capacitor with superior anti-self-discharge function, ACS Nano 13 (2019) 8275–8283.
[60] C.J. Zhang, S. Pinilla, N. McEvoy, C.P. Cullen, B. Anasori, E. Long, S.-H. Park, A. Seral-Ascaso, A. Shmeliov, D. Krishnan, C. Morant, X. Liu, G.S. Duesberg, Y. Gogotsi, V. Nicolosi, Oxidation stability of colloidal two-dimensional titanium carbides (MXenes), Chem. Mater. 29 (2017) 4848–4856.
[61] X. Xie, M.-Q. Zhao, B. Anasori, K. Maleski, C.E. Ren, J. Li, B.W. Byles, E. Pomerantseva, G. Wang, Y. Gogotsi, Porous heterostructured MXene/carbon nanotube composite paper with high volumetric capacity for sodium-based energy storage devices, Nano Energy 26 (2016) 513–523.
[62] Y. Xiao, J.-Y. Hwang, I. Belharouak, Y.-K. Sun, Superior Li/Na-storage capability of a carbon-free hierarchical CoS_x hollow nanostructure, Nano Energy 32 (2017) 320–328.
[63] D. Ji, L. Fan, L. Li, S. Peng, D. Yu, J. Song, S. Ramakrishna, S. Guo, Atomically transition metals on self-supported porous carbon flake arrays as binder-free air cathode for wearable zinc-air batteries, Adv. Mater. 31 (2019) 1808267.
[64] X.L. Huang, C. Zhou, W. He, S. Sun, Y.-L. Chueh, Z.M. Wang, H.K. Liu, S.X. Dou, An emerging energy storage system: advanced Na-Se Batteries, ACS Nano 15 (2021) 5876–5903.
[65] S. Zhang, H. Ying, P. Huang, J. Wang, Z. Zhang, T. Yang, W.-Q. Han, Rational design of pillared SnS/$Ti_3C_2T_x$ MXene for superior lithium-ion storage, ACS Nano 14 (2020) 17665–17674.
[66] Y. Liu, F. Wang, L.-Z. Fan, Self-standing Na-storage anode of Fe_2O_3 nanodots encapsulated in porous N-Doped carbon nanofibers with ultra-high cyclic stability, Nano Res. 11 (2018) 4026–4037.
[67] Y. Fang, Y. Zhang, C. Miao, K. Zhu, Y. Chen, F. Du, J. Yin, K. Ye, K. Cheng, J. Yan, G. Wang, D. Cao, MXene-derived defect-rich TiO_2@rGO as high-rate anodes for full Na ion batteries and capacitors, Nano-Micro Lett. 12 (2020) 128.
[68] P. Huang, S. Zhang, H. Ying, Z. Zhang, W. Han, Few-Layered Ti_3C_2 MXene anchoring bimetallic selenide $NiCo_2Se_4$ nanoparticles for superior sodium-ion batteries, Chem. Eng. J. 417 (2021), 129161.
[69] T. Zhou, C. Wu, Y. Wang, A.P. Tomsia, M. Li, E. Saiz, S. Fang, R.H. Baughman, L. Jiang, Q. Cheng, Super-tough MXene-functionalized graphene sheets, Nat. Commun. 11 (2020) 2077.
[70] W.-S. Wang, D.-H. Wang, W.-G. Qu, L.-Q. Lu, A.-W. Xu, Large ultrathin anatase TiO2 nanosheets with exposed 001 facets on graphene for enhanced visible light photocatalytic activity, J. Phys. Chem. C 116 (2012) 19893–19901.
[71] Y. Fang, D. Luan, Y. Chen, S. Gao, X.W.D. Lou, Synthesis of copper-substituted CoS_2@Cu_xS double-shelled nanoboxes by sequential ion exchange for efficient sodium storage, Angew. Chem., Int. Ed. 59 (2020) 2644–2648.
[72] F. Xiao, X. Yang, H. Wang, D.Y.W. Yu, A.L. Rogach, Hierarchical CoS_2/N-doped carbon@MoS_2 nanosheets with enhanced sodium storage performance, ACS Appl. Mater. Interfaces 12 (2020) 54644–54652.
[73] X. Wang, X. Li, Q. Li, H. Li, J. Xu, H. Wang, G. Zhao, L. Lu, X. Lin, H. Li, S. Li, Improved electrochemical performance based on nanostructured SnS_2@CoS_2-rGO composite anode for sodium-ion batteries, Nano-Micro Lett. 10 (2018) 46.
[74] X. Ge, Z. Li, L. Yin, Metal-organic frameworks derived porous core/shell CoP@C polyhedrons anchored on 3D reduced graphene oxide networks as anode for sodium-ion battery, Nano Energy 32 (2017) 117–124.
[75] X. Wang, S. Kajiyama, H. Iinuma, E. Hosono, S. Oro, I. Moriguchi, M. Okubo, A. Yamada, Pseudocapacitance of MXene nanosheets for high-power sodium-ion hybrid capacitors, Nat. Commun. 6 (2015) 6544.
[76] X. Guo, J. Zhang, J. Song, W. Wu, H. Liu, G. Wang, MXene encapsulated titanium oxide nanospheres for ultra-stable and fast sodium storage, Energy Storage Mater. 14 (2018) 306–313.
[77] X. Ou, C. Yang, X. Xiong, F. Zheng, Q. Pan, C. Jin, M. Liu, K. Huang, A New rGO-overcoated Sb_2Se_3 nanorods anode for Na^+ battery. in situ X-Ray diffraction study on a live sodiation/desodiation process, Adv. Funct. Mater. 27 (2017) 1606242.
[78] Z. Wu, G. Liang, W.K. Pang, T. Zhou, Z. Cheng, W. Zhang, Y. Liu, B. Johannessen, Z. Guo, Coupling topological insulator $SnSb_2Te_4$ nanodots with highly doped graphene for high-rate energy storage, Adv. Mater. 32 (2020) 1905632.
[79] Y. Zhang, N. Wang, P. Xue, Y. Liu, B. Tang, Z. Bai, S. Dou, Co_9S_8@carbon nanospheres as high-performance anodes for sodium ion battery, Chem. Eng. J. 343 (2018) 512–519.
[80] Z. Hu, X. Kuai, J. Chen, P. Sun, Q. Zhang, H.H. Wu, L. Zhang, Strongly coupled MoS_2 nanocrystal/Ti_3C_2 nanosheet hybrids enable high-capacity lithium-ion storage, ChemSusChem 13 (2020) 1485–1490.
[81] J. Song, S. Qiu, F. Hu, Y. Ding, S. Han, L. Li, H.Y. Chen, X. Han, C. Sun, S. Peng, Sub-2 nm thiophosphate nanosheets with heteroatom doping for enhanced oxygen electrocatalysis, Adv. Funct. Mater. 31 (2021) 2100618.
[82] J. Xie, P. Yang, Y.i. Wang, T. Qi, Y. Lei, C.M. Li, Puzzles and confusions in supercapacitor and battery: theory and solutions, J. Power Sources 401 (2018) 213–223.